Overcoming surface energy to control Cu_3N epitaxial growth

Zainab Fatima[1], Isao Ohkubo[1,3,*], Satoshi Ishii[1,3], Takahiro Nagata[2], Takashi Aizawa[1], Takao Mori[1,3]

[1.] Research Center for Materials Nanoarchitectonics (MANA), National Institute for Materials Science (NIMS), 1-1 Namiki, Tsukuba, Ibaraki 305-0044, Japan

[2.] Research Center for Electronic and Optical Materials, National Institute for Materials Science (NIMS), 1-1 Namiki, Tsukuba, Ibaraki 305-0044, Japan

[3.] Department of Materials Science, Institute of Pure and Applied Sciences, University of Tsukuba, 1-1-1 Tennodai, Tsukuba, Ibaraki 305-8573, Japan

[*] Corresponding author: OHKUBO.Isao@nims.go.jp

ABSTRACT

Crystal orientation control during copper nitride (Cu_3N) epitaxial growth was achieved using reactive DC magnetron sputtering. Both the (100)-orientation and (111)-orientation were observed readily from X-ray diffraction measurements for Cu_3N thin films grown on single-crystal MgO(100), MgO(111), $SrTiO_3$(100), and sapphire(0001) substrates. The Cu_3N(111) surface energy is greater than that of Cu_3N(100), suggesting that the Cu_3N(111) orientation has a lower formation probability than the Cu_3N(100) orientation. To control the influence of surface energy, thin film growth parameters related to the thermodynamics and kinetics of epitaxial thin film growth were tuned. Growth of single (111)-oriented Cu_3N epitaxial thin films, which has a higher surface energy orientation, was achieved on MgO(111) substrates. Optical band gaps of the single (111)-oriented Cu_3N epitaxial thin film were 1.80 eV for direct transition and 0.82 eV for indirect transition, indicating formation of a reasonable electronic structure in single (111)-oriented Cu_3N epitaxial thin films with higher surface energy.

1. INTRODUCTION

Thin film growth is a crystal growth process by which a vapor-phase species adsorbs onto a single-crystal substrate, leading to formation of a crystal lattice aligned under the influence of the substrate surface lattice. This process is driven both thermodynamically and kinetically because the system tends toward minimizing its energy while enabling atomic rearrangement through surface mobility.[1] Production of crystal-oriented thin films, i.e., epitaxial thin films, requires that a fine balance be achieved among chemical reactivity, thermal activation, and crystallographic lattice matching at the film-substrate interface.[1] For many research studies today, phase-pure and orientation-pure epitaxial thin films are necessary. During the initial growth stage of thin film formation, the surface energies and the nucleation process on a substrate can be expected to influence the crystal orientation of a thin film.[2–4] Moreover, crystal orientation stability includes surface energy effects. Therefore, to achieve phase-pure and orientation-pure epitaxial thin film growth, the crystal orientation stability should be controlled by tuning the thin film epitaxial growth parameters associated with thermodynamics and kinetics.[3–6]

In this regard, copper nitride (Cu_3N), which is a particularly intriguing material with a cubic anti-ReO_3 structure, has attracted attention for various applications.[7–9] The thin film growth of Cu_3N has been investigated using various growth techniques.[10–27] Actually, Cu_3N is prone to decomposition into Cu and N_2, necessitating careful control of process parameters such as the growth temperature and nitrogen partial pressure, to stabilize the desired phase.[12] Among various thin film growth techniques, sputtering is more controlled in terms of kinetics than either molecular beam epitaxy (MBE) or chemical vapor deposition (CVD) because of the high kinetic energies of supply species from the sputtering target.[28] Therefore, process parameters such as the sputtering power, gas pressure, and growth rate influence the energy and supply species, leading to thin film formation. For example, high growth rates might favor amorphous or polycrystalline films because of limited surface diffusion and growth temperature, whereas optimized growth rates and substrate heating can promote crystallinity and preferred orientations.

Surface energy is another parameter that must be considered when elucidating the growth dynamics.[2–4] Preferential growth of certain crystallographic orientations (100) or (111) textured domains is influenced by minimization of the surface and interfacial energies. For instance, low-energy surfaces predominate under normal conditions, but kinetic limitations (e.g., limited surface species mobility) can allow them to generate higher-energy surfaces. Additionally, differences in surface energy between the film and the substrate can lead to island formation, coalescence, and overall film roughness.[29]

For this study, the growth of Cu_3N thin films by reactive DC magnetron sputtering is assessed on various single-crystal substrates, with specific examination of how thermodynamics, kinetics, and surface energy determine the Cu_3N thin films' crystallographic orientation. By varying growth parameters such as the growth temperature, growth rate, nitrogen gas pressure, and sputtering power, we can elucidate their roles in stabilizing the Cu_3N phase when controlling crystallographic orientation. These insights not only advance the fundamental understanding of nitride thin film synthesis: they are also necessary for achieving epitaxial growth and for tailoring film properties.

2. EXPERIMENTAL

The Cu_3N thin films used for this study were grown using reactive DC magnetron sputtering equipment (Kenix Co. Ltd.) with a 99.99% pure Cu target. Single-crystal sapphire(0001) (Cryscore Optoelectronic Ltd.), $SrTiO_3$(100) (Shinkosha Co. Ltd.), MgO(111) and MgO(100) substrates produced by CrysTec GmbH were used to assess thin film growth. All the substrates were preheated in a vacuum for 10–30 min using a lamp heater at 800 °C. The typical base pressure of the sputtering chamber was maintained on the order of 10^{-7} Pa. The DC power was 25–50 W. The sputtering gas was 99.999% pure nitrogen in the optimum range of 0.3–2.3 Pa. Its flow rate was 3–10 sccm. The separation distance between the target and substrate was 60–70 mm. Cu_3N thin films were grown at temperatures of 110–200 °C with growth rates of 0.15–1.0 Å/s because Cu_3N decomposes at 260 °C.[10,17] Structural evaluations of Cu_3N thin films were performed based on X–ray diffraction

(XRD) measurements using a four-axis diffractometer (D8; Bruker Analytik GmbH) with Cu $K_{\alpha 1}$ radiation and a high-resolution two-dimensional (2D) detector. The 2D detector system can detect parts of the Debye–Scherrer ring rapidly and two-dimensionally with a psi (ψ) angle range of about 30°. The conventional 2θ–ω chart is obtained by integrating the 2D scan image in the ψ direction. The film thicknesses were measured using a surface profilometer (Dektak XT; Bruker Analytik GmbH). Chemical depth analysis of Cu_3N thin films was performed using ex-situ Auger electron spectroscopy (AES). The surface characterization apparatus, which had base pressure in the 10^{-8} Pa range, was equipped with a cylindrical mirror analyzer for AES and an ion gun for sputter etching.[30,31] For Auger electron excitation, the 15 keV electron beam was focused on the normal surface of Cu_3N thin films at an angle of incidence of 70°. Sputter etching was performed with 3 keV Kr^+ ions at about 5 μA and with the angle of incidence of 45°. Surface morphologies of Cu_3N thin films were characterized using atomic force microscopy (AFM, AFM5300E; Hitachi High-Technologies Corp.). Optical band gaps of epitaxial Cu_3N thin films were characterized based on their absorptivity, obtained through spectroscopic ellipsometry measurements (SE 850; Sentech Instruments GmbH) at room temperature. The Tauc–Lorentz model[32] was used to fit the ellipsometry spectra. Electronic structure calculations were performed using density-functional theory (DFT) through a full-potential linearized augmented plane-wave approach implemented in the WIEN2k code.[33] The modified Becke–Johnson (mBJ) potential[34, 35] was employed. Energy band gaps (E_g) calculated using the mBJ potential are much closer to the experimentally obtained values than those from the generalized gradient approximation (GGA) functional potential and local density approximation (LDA).[34–36] Parameter $R_{mt}K_{max}$, where R_{mt} represents the smallest muffin-tin radius, and where K_{max} denotes the plane-wave cutoff, was used to control the basis set size: this parameter was set to the high value of 7.0. For the atomic spheres, the R_{mt} values were 1.97 for Cu and 1.61 for N. In addition, to calculate the electronic structure, 100 k-points in the Brillouin zone were used. Convergence was reached with k-point sampling of 100. For the DFT calculations, we used

structural coordinates and lattice parameters[9] of Cu_3N obtained from X-ray diffraction measurements.

3. RESULTS and DISCUSSION

Figure 1 shows typical XRD 2D images and 2θ–ω patterns of Cu_3N thin films grown on single-crystal sapphire(0001), $SrTiO_3$(100), MgO(111), and MgO(100) substrates at growth temperatures of 170–180 °C. On all substrates, multiple XRD diffraction peaks were observed with various crystallographic orientations originating from the Cu_3N phase, indicating that the thin films are Cu_3N polycrystalline. Whereas (100)-oriented growth of Cu_3N is typically favored on cubic substrates such as MgO(100) and $SrTiO_3$(100), strong (111) diffraction peaks were observed in both cases. By contrast, on sapphire(0001) substrates, where (111) orientation of Cu_3N was anticipated because of rhombohedral symmetry, dominant (100) diffraction peaks were observed.[11] For the MgO(111) substrates, (111) orientation peaks of Cu_3N were dominant, but were accompanied by other orientation peaks. These behaviors are more or less consistent with most previously reported Cu_3N thin film growth on glass and various single-crystal substrates, where peaks of (111)-oriented Cu_3N tend to be observed in addition to a peak of (100)-oriented Cu_3N, irrespective of the thin film growth method which was used.[13,15,19,23–26] However, Cu_3N thin films produced using pulsed laser deposition show the (111) preferential growth of Cu_3N on Si(111) substrates.[14] This growth suggests that the preferential growth orientation of Cu_3N depends on the growth methods and conditions. The lattice constant values of Cu_3N thin films obtained from XRD patterns presented in Fig. 1 were 3.828 Å for the (100) orientation and 3.826 Å for the (111) orientation on MgO(100) substrate, 3.820 Å for the (111) orientation on $SrTiO_3$(100) substrate, 3.827 Å for both (100) and (111) orientations on sapphire(0001) substrate, 3.822 Å for (100) orientation and 3.827 Å for (111) orientation on MgO(111) substrate. Comparison of these values to the bulk lattice constant of 3.819 Å[9] shows that the lattice constant differences are 0.03–0.24%, suggesting that the Cu and N ratios might be approximately equal to the stoichiometric composition. Auger electron spectra of Cu_3N thin films

in the depth direction are portrayed in Fig. S1. In addition to Cu peaks, very weak carbon and oxygen peaks were observed. As portrayed in an AFM image of the Cu_3N thin film surface presented in Fig. S2, the origins of these carbon and oxygen peaks are regarded as residual carbon and oxygen in the depressions of Cu_3N thin film surfaces. Details of AES spectra are presented in the supplementary material. The influences of oxygen and carbon impurities are sufficiently small in this study.

For thin film growth, surface energy should play a central role in dictating the morphology, crystalline orientation, and overall structural quality of thin films.[2-4] In fact, surface energy is associated with atoms near the surface because of their under-coordinated bonding environment compared to the bulk. For this study, surface energy ($Y_{(hkl)}$) was calculated using the equation derived by Holzer, Tielemann, and Müller *et al*.[37,38] as shown below.

$$Y_{(hkl)} = \frac{1}{N_a} \Sigma \frac{S_{(hkl)}\, D^{\circ}}{A_{(hkl)}} \qquad (1)$$

Therein, N_a is Avogadro's constant, $S_{(hkl)}$ represents the number of broken metal cation–anion bonds in $A_{(hkl)}$, where $A_{(hkl)}$ stands for the (hkl) surface area of the surface unit cell. In addition, D° denotes the bond energy. Actually, $A_{(hkl)}$ is calculated from the crystal structure data[9,39–41] presented in Table 1. For this study, the D° values were calculated from the formation enthalpies (ΔH_f°) of crystal and gas phases for metal cation (M), anion (X), and a solid compound (MX) using the thermochemical equation[42,43] as

$$D°(\text{M-X}) = \Delta H_f^{\circ}(\text{M}) + \Delta H_f^{\circ}(\text{X}) - \Delta H_f^{\circ}(\text{MX}). \qquad (2)$$

The values of ΔH_f° at 298.15 K were referred from an earlier report of the literature.[44] The ΔH_f° values used for calculating the bond energy (D°) via thermochemical cycles are presented in Table S1 of the supplementary material. Table 1 presents the calculated surface energies of (100) and (111) planes of Cu_3N and some ionic metal oxides. Surface energies obtained from this calculation tend to be greater than those obtained from DFT calculations reported earlier. The surface energies of the (111) plane in Cu_3N and MgO with cubic crystal structures tend to be larger than those of the (100) plane. The (111) surface energies of various rock salt type crystal structure compounds such as

MgO(111) and Cu_3N tend to be sufficiently larger than those of (100) plane surface energies, indicating that the (111) surfaces of rock salt type compounds and Cu_3N are regarded as having lower stability than their (100) surfaces,[45,46,50] which are consistent with the trend of this calculation. The calculated surface energy of the (111) plane of Cu_3N is higher than that of the Cu_3N(100) surface, but both the (100)-orientation and (111)-orientation of Cu_3N are generated during thin film growth, as depicted in Fig. 1. This finding implies that the (111)-Cu_3N orientation probability is approximately equal to that of the (100)-Cu_3N orientation probability. During the thin film growth of Cu_3N using the reactive DC magnetron sputtering method, the (111)-oriented Cu_3N growth was promoted by overcoming the influence of high surface energy. Table 1 also presents the surface energies of the substrates used for this study.

To investigate the influence of a substrate on the (111)-orientation and (100)-orientation in Cu_3N layers, XRD phi (φ) scan measurements were taken. Figure 2 shows the XRD φ scan patterns of the majority orientations of Cu_3N layers grown on the MgO(100) and MgO(111) substrates. As depicted in Figs. 1(a) and 1(d), the majority orientations of Cu_3N layers are (100) of Cu_3N for the MgO(100) substrate, (111) of Cu_3N for the MgO(111) substrate. The second-largest XRD intensity orientations are the (111)-orientation of Cu_3N for the MgO(100) substrate, and the (100)-orientation of Cu_3N for the MgO(111) substrate. For the second-largest XRD intensity orientations, taking XRD φ scan measurements was difficult because of their weak XRD peak intensities and broadening along the ψ direction, indicating the large mosaicities of these domain rotations, as portrayed in the XRD 2D images of Fig. 1. The XRD φ scan patterns in Fig. 2 were obtained from the same samples as those shown in Figs. 1(a)(b) and 1(g)(h). In the Cu_3N layer grown on the MgO(100) substrate, fourfold symmetric peaks of Cu_3N{111} diffraction were observed (Fig. 2(a)). By contrast, in the Cu_3N layer grown on the MgO(111) substrate, threefold symmetric peaks of Cu_3N{111} were observed (Fig. 2(c)). Bump-like weak peaks observed between the neighboring sharp peaks in Fig. 2(c) originate from the broadened reciprocal lattice point because of the large mosaicity along the ψ direction of the second-largest XRD intensity orientations. The in-plane crystallographic epitaxial

relations of the majority orientations are (100)Cu_3N//(100)MgO and [010]Cu_3N//[010]MgO for the Cu_3N thin film on the MgO(100) substrate and (111)Cu_3N//(111)MgO and $[1\bar{1}0]Cu_3N$//$[1\bar{1}0]$MgO for the Cu_3N thin film on the MgO(111) substrate, which indicates that the Cu_3N majority orientations were grown under the strong influence of the MgO substrate surface lattices. However, the second-largest XRD intensity orientations are regarded as growing under conditions of lesser influence of the MgO substrate surface lattices because of the large mosaicities of the domain rotation along the ψ directions (Figs. 1(a) and 1(g)). The lattice mismatch values between Cu_3N (a cubic anti-ReO_3 structure, a = 3.819 Å[9]) and MgO (a cubic rock salt crystal structure, a = 4.213 Å[39]) substrates are approximately 9.35% for both between Cu_3N(100) and MgO(100), and between Cu_3N(111) and MgO(111). On MgO(100) substrates, the second-largest XRD intensity orientations of Cu_3N(111) have a surface unit cell with rhombohedral symmetry, whereas the surface unit cell of the MgO(100) substrate has cubic symmetry. Similarly, on MgO(111) substrates, the surface unit cell of the second-largest XRD intensity orientations for Cu_3N(100) has cubic symmetry, whereas the surface unit cell of the MgO(111) substrate has rhombohedral symmetry. Because the surface unit cell symmetries of the second-largest XRD intensity orientations and MgO substrates mutually differ, the second-largest XRD intensity orientations are regarded as growing irrespective of the substrate surface lattice influences. Although the majority orientations grew under the influence of the substrate surface lattices, both the second-largest XRD intensity (100)-orientation and (111)-orientation of Cu_3N grew despite their surface energies and the MgO substrate surface lattice symmetries.

To control epitaxial thin film growth, the effects of thermodynamics and kinetics should be considered. To this end, the growth temperature and growth rate effects are evaluated using analyses of XRD 2θ–ω patterns. All the XRD peak intensities originating from Cu_3N layers are normalized by both the film thickness d and substrate XRD peak intensities, i.e., $I_{norm}^{(111)} = I_{film}^{(111)} / (I_{substrate}\, d)$.[51,52] The following equation was used to evaluate the intensity ratio of the summation of Cu_3N(111) and (222) peaks to the sum of the XRD peak intensities of all Cu_3N.

$$I_R^{(111)+(222)} = \frac{I_{norm}^{(111)} + I_{norm}^{(222)}}{\Sigma I_{norm}^{(hkl)}} \qquad (3)$$

Therein, $I_{norm}^{(111)}$ and $I_{norm}^{(222)}$ respectively represent the normalized XRD intensity peaks of Cu_3N(111) and (222). In addition, $\Sigma I_{norm}^{(hkl)}$ represents the summation of intensities of all Cu_3N XRD peaks. The ratio is represented by $I_R^{(111)+(222)}$. To elucidate the influence of growth parameters on the crystallographic orientation of Cu_3N thin films, $I_R^{(111)+(222)}$ as a function of the growth temperature and growth rate is discussed. In this case, the XRD 2θ–ω patterns of 52 samples obtained on MgO(100), $SrTiO_3$(100), sapphire(0001), and MgO(111) substrates are used. The results demonstrate that $I_R^{(111)+(222)}$ depends on the growth temperature and growth rate, as shown in Figs. 3 and 4. In addition, $I_R^{(111)+(222)}$ tends to decrease as the growth temperature increases. Moreover, it exhibits a maximum value at a growth rate of 0.33 Å/s. Below that growth rate of 0.33 Å/s, $I_R^{(111)+(222)}$ tends to decrease. As shown in Fig. S3, the growth rate showed a tendency to remain largely unchanged at growth temperatures of 110 °C to 200 °C at the constant of other growth parameters. Orientation-pure, single (111)-oriented Cu_3N epitaxial thin films have been obtained at the low growth temperature of 110 °C and low growth rate of 0.33 Å/s ($I_R^{(111)+(222)} = 1$). This growth condition is an appropriate growth condition to achieve a higher formation probability of Cu_3N (111)-orientation possessing large surface energy, in which the balance between thermodynamics and kinetics is tuned.

By contrast, the behaviors of $I_R^{(100)+(200)}$ for the growth temperature and the growth rate differ from those of $I_R^{(111)+(222)}$ as shown in Figs. 3 and 4. Even though the surface energy of Cu_3N(100) is less than that of Cu_3N(111), the values of $I_R^{(100)+(200)}$ are low, with a maximum value of 0.67. The variations in the values of $I_R^{(100)+(200)}$ to the growth temperature and the growth rate tend to be small compared to those of $I_R^{(111)+(222)}$. This result indicates that, in the reactive DC magnetron sputtering, the formation probability of Cu_3N(111) orientation with larger surface energy

remains as well as that of $Cu_3N(100)$ orientation with smaller surface energy. Actually, $SrTiO_3(100)$ (a = 3.905 Å[41]) substrate is a promising substrate for $Cu_3N(100)$ growth because of its small lattice mismatch with $Cu_3N(100)$ of 2.2%. However, the $I_R^{(100)+(200)}$ values found from this study are low even with the $SrTiO_3(100)$ substrate. The formation of crystal nuclei with high surface energy orientations is regarded as suppressed at the initial thin film growth stage because of their instability. However, with Cu_3N thin film growth via reactive DC magnetron sputtering, high surface energy crystal orientations are formed. This study presents an example that overcomes the relation between the preference for out-of-orientation in thin film growth and the stability of the resultant surface. Additional effects on Cu_3N thin film growth are surface reconstruction effects of Cu_3N and substrates, along with non-charge-neutrality effects of $Cu_3N(111)$ and $MgO(111)$ substrate surfaces. Further detailed research must be undertaken to elucidate these effects on Cu_3N thin film growth.

For this study, pure (111)-oriented Cu_3N epitaxial thin films were grown on $MgO(111)$ substrates with a growth temperature of 110 °C and a growth rate of 0.33 Å/s by adjusting the balance between thermodynamics and kinetics. A strong and sharp (111) diffraction peak from the Cu_3N thin film is visible, aligned with the (111) peak of the MgO substrate, as shown in Figs. 5(a) and 5(b). The absence (or marked suppression) of other Cu_3N orientations in the XRD diffraction pattern supports the epitaxial characteristics of the growth. The lattice constant obtained for the Cu_3N thin film is 3.814 Å with 0.12% expansion, compared to the bulk lattice constant.[9] The fairly good lattice mismatch (9.35%) and surface atomic configuration symmetry between $Cu_3N(111)$ and $MgO(111)$ facilitate this orientation. Single orientation along the in-plane direction was also found from XRD φ scanning measurements, as shown in Figs. 5(c) and 5(d), corresponding to the in-plane epitaxial relation of $Cu_3N[1\bar{1}0]$//$MgO[1\bar{1}0]$. The XRD intensity of $Cu_3N\{111\}$ peaks in the φ scan pattern for the single (111)-oriented epitaxial Cu_3N thin film is much greater than the intensity found for the polycrystalline Cu_3N thin film grown on a $MgO(111)$ substrate, as presented in Fig. 2(c). The noise level in the XRD φ scan pattern of the single (111)-oriented epitaxial Cu_3N thin film (Fig. 5(c)) is much lower than that of the polycrystalline Cu_3N thin film presented in Fig. 2(c).

By contrast, single (100)-oriented Cu_3N epitaxial thin films were fabricated on $SrTiO_3$(100) substrates using molecular beam epitaxy.[18] Generally speaking, the energy range of the supply species used with sputtering methods (order of 10 eV)[28] is much greater than that of supply species used with molecular beam epitaxy methods (thermal energy on the order of 0.1 eV).[1] Therefore, thin films produced using molecular beam epitaxy are grown under conditions closely approximating thermodynamic conditions, whereas thin films produced by sputtering are grown under conditions that differ greatly from thermodynamic conditions. In addition to the energy of supply species, with molecular beam epitaxy, supply species reach substrate surfaces by maintaining their mean free path in sufficiently high-vacuum conditions. Consequently, the supply species are Cu atom species and N atom species. By contrast, with reactive DC magnetron sputtering, the supply species might be Cu_xN_y in addition to Cu-related and N-related species with higher energies under high N_2 gas pressures on the order of several pascals.[53] Differences in supply species might also influence the crystal orientation control. In addition to the differences in supply species and their energies, the surface energies on crystal growth differ according to their growth conditions and growth methods.[2,4] Therefore, for the reactive DC magnetron sputtering thin film growth, it can be inferred that the formation probability of (111)-orientation of Cu_3N with large surface energy exists in addition to the (100)-orientation formation probability, irrespective of substrate surface unit cell symmetry.

Optical absorption spectra of the single (111)-oriented Cu_3N epitaxial film grown on a MgO(111) substrate, as obtained by spectroscopic ellipsometry measurements, are presented in Fig. 6(a). The direct band gap was obtained by plotting the $(\alpha\hbar\omega)^2$ versus $\hbar\omega$ (energy) curve and by extrapolating the full line to the horizontal axis of $\hbar\omega$. Similarly, the indirect band gap was found by extrapolating the full line to the horizontal line of $\hbar\omega$ in the $(\alpha\hbar\omega)^{1/2}$ versus $\hbar\omega$ curve. The direct and indirect band gap values were found respectively as 1.80 and 0.82 eV. Various values for the optical band gap of Cu_3N have been reported to date. Experimentally obtained values for optical band gaps have been reported as 1.3–1.7 eV,[16] 1.44 eV,[24] 1.5–1.8 eV,[19] 1.57 eV,[15] 1.65 eV,[12] 1.68 eV,[21] 1.7 eV,[22] 1.7–1.9 eV,[25] 1.72–2.38 eV,[20] 1.8 eV,[11] 2.14 eV, and 2.21 eV[26] for direct optical band gaps, and as

1.0 eV,[22] 1.17–1.68 eV,[20] 1.3 eV,[18] 1.45 eV, and 1.46 eV[26] for indirect optical band gaps. The values of the direct and indirect optical band gaps obtained from this study are reasonably consistent with those reported from most of the earlier studies conducted on this subject. The direct and indirect optical band gaps of Cu_3N obtained from this study are discussed by comparing them with the electronic band structure calculated using DFT, as presented in Fig. 6(b). The electronic band structure in Fig. 6(b) shows similar trends to those reported earlier.[21,24,54,55] The direct transition band gap is apparent between the R points, with a value of 1.21 eV. The electronic structure was calculated using mBJ, which provides improved band gap values compared to DFT calculations using LDA and GGA-PBE. However, even the band gap values obtained using mBJ calculations generally tend to show smaller band gaps than the experimentally obtained values.[34–36] Therefore, this relation is consistent with the direct optical band gap of 1.80 eV obtained from this study. In Fig. 6(b), the indirect band gaps between the Γ (conduction band minimum, CBM)–R (valence band maximum, VBM) points and between the M (CBM)–R (VBM) points are apparent, respectively, with values of 1.08 eV and 0.41 eV. The indirect optical band gap of 0.82 eV observed in Fig. 6(a) is regarded as attributable to these indirect transitions in Fig. 6(b). The two broad peaks observed at the low energy side of the $(\alpha\hbar\omega)^{1/2}$ versus the $\hbar\omega$ curve in Fig. 6(a) were also reported earlier in the literature.[21,24,26] The origin of these absorption peaks remains unclear. One possible explanation is absorption because of the energy levels formed within the band gap, caused by factors such as defects or impurities.[22,55–57] More-detailed studies must be conducted to elucidate these two broad absorption peaks. The optical bandgap for direct transition is larger than the value obtained by DFT calculation. In contrast, the optical bandgap for indirect transition was similar to the values calculated using DFT. One factor that might be related to this point is the influence of the functionals on DFT calculations. On the lowest conduction band, the energy level at the Γ point for mBJ is lower than that at the R point, whereas the energy level at the Γ point is higher than that at the R point for GGA-PBE, as presented in Fig. S5 and Table S2. Changes in band structures attributable to functional differences have been reported,[58–63] as described in detail in the supplementary material. Comparison of the

optical absorption spectra with the electronic band structure calculated using DFT indicates that the single (111)-oriented Cu_3N epitaxial films grown on MgO(111) substrates form an appropriate electronic structure, thereby indicating the high-crystalline quality epitaxial thin films.

4. CONCLUSION

In conclusion, thin film growth of Cu_3N by reactive DC magnetron sputtering was conducted on MgO(100), $SrTiO_3$(100), sapphire(0001), and MgO(111) substrates. Irrespective of the substrate, a tendency to form polycrystalline orientations of Cu_3N phases was observed. The dominant crystalline orientations of Cu_3N were (111) and (100) orientations, although the surface energy of Cu_3N(111) is higher than that of Cu_3N(100). By tuning the parameters of thermodynamics and kinetics affecting thin film growth, single (111)-oriented Cu_3N epitaxial thin films were obtained on MgO(111) substrates, which possess high surface energy. Optical direct-band and indirect-band gaps of 1.80 eV and 0.82 eV in the single (111)-oriented Cu_3N epitaxial thin film were observed based on spectroscopic ellipsometry measurements, which are reasonably consistent with values presented in most earlier reports. This study has highlighted the importance of the following points. For thin film growth, even a crystal orientation with high surface energy can be grown stably because the surface energy varies with growth conditions and growth methods, in addition to temperatures, absorption, and other parameters. Such single-oriented epitaxial thin films are producible by tuning the balance between thermodynamics and kinetics during thin film growth and by selecting an appropriate substrate.

SUPPLEMENTARY MATERIAL

See the supplementary material for AES spectra, AFM image, thermochemical cycles and formation enthalpies for calculating the bond energy, growth rate of Cu_3N thin films shown as a function of growth temperature, XRD 2θ–ω patterns of a Cu_3N(111) epitaxial thin film grown on MgO(111) substrate, and of a bare MgO(111) substrate, electronic band structures of Cu_3N calculated by mBJ exchange potential and GGA-PBE exchange-correlation functional, and raw data of spectroscopic ellipsometry measurements (amplitude ratio (Ψ), phase change (Δ), complex refractive indices (ε_1 and ε_2), refractive index (n), extinction coefficient (k), and absorption coefficient (α)).

ACKNOWLEDGMENTS

This work was supported by funding from JSPS-KAKENHI (no. 23H00263) and the JST–Mirai Program (JPMJMI19A1). We thank Ms. Tomoko Kobayashi for AFM measurements.

AUTHOR DECLARATIONS

Conflict of Interest

The authors have no conflict to disclose.

Author Contributions

Zainab Fatima: Investigation (equal); Data curation (equal); Formal analysis (equal); Writing/original draft preparation (equal). **Isao Ohkubo:** Conceptualization (equal); Methodology (equal); Investigation (equal); Data curation (equal); Formal analysis (equal); Writing/original draft preparation (equal); Project administration (equal); Funding acquisition (equal). **Satoshi Ishii:** Methodology (equal); Resources (equal); Investigation (equal); Data curation (equal); Formal analysis (equal); Writing/review & editing (supporting). **Takahiro Nagata:** Methodology (equal); Resources (equal); Investigation (equal); Data curation (equal); Formal analysis (equal); Writing/review & editing (supporting). **Takashi Aizawa:** Conceptualization (equal); Methodology (equal); Investigation (equal); Writing/review & editing (equal). **Takao Mori:** Resources (equal); Writing/review & editing (supporting); Supervision (equal); Project administration (equal); Funding acquisition (equal).

DATA AVAILABILITY

Data supporting the findings of this study are available within the article and its supplementary material, and upon reasonable request from the corresponding author.

REFERENCES

1. M. A. Herman, W. Richter, and H. Sitter, *Epitaxy: Physical Principles and Technical Implementation* (Springer Berlin Heidelberg, 2004).
2. H. Yoshiyama, S. Tanaka, Y. Mikami, S. Ohshio, J. Nishiura, H. Kawakami, and H. Kobayashi, "Role of surface energy in thin-film growth of electroluminescent ZnS, CaS and SrS," J. Cryst. Growth **86**, 56–60 (1988).
3. N. Fujimura, T. Nishihara, S. Goto, J. Xu, and T. Ito, "Control of preferred orientation for ZnO_x films: control of self-texture," J. Cryst. Growth **130**, 269–279 (1993).
4. C. Körber, J. Suffner, and A. Klein, "Surface energy controlled preferential orientation of thin films," J. Phys. D: Appl. Phys. **43**, 055301 (2010).
5. I. Ohkubo, A. Ohtomo, T. Ohnishi, Y. Matsumoto, H. Koinuma, and M. Kawasaki, "In-plane and polar orientations of ZnO thin films grown on atomically flat sapphire," Surf. Sci. **443**, L1043–L1048 (1999).
6. I. Ohkubo, T. Aizawa, K. Nakamura, and T. Mori, "Control of competing thermodynamics and kinetics in vapor phase thin-film growth of nitrides and borides," Front. Chem. **9**, 642388 (2021).
7. H. A. Evans, Y. Wu, R. Seshadri, and A. K. Cheetham, "Perovskite-related ReO_3-type structures," Nat. Rev. Mater. **5**, 196–213 (2020).
8. R. Juza and H. Hahn, "Über die kristallstrukturen von Cu_3N, GaN und InN metallamide und metallnitride," Z. Anorg. Allg. Chem. **239**, 282–287 (1938).
9. U. Zachwieja and H. Jacobs, "Ammonothermalsynthese von kupfernitrid Cu_3N," J. Less-Common Met. **161**, 175–184 (1990).
10. M. Asano, K. Umeda, and A. Tasaki, "Cu_3N thin film for a new light recording media," Jpn. J. Appl. Phys. **29**, 1985–1986 (1990).

11. T. Nosaka, M. Yoshitake, A. Okamoto, S. Ogawa, and Y. Nakayama, "Copper nitride thin films prepared by reactive radio-frequency magnetron sputtering," Thin Solid Films **348**, 8–13 (1999).
12. D. M. Borsa, S. Grachev, C. Presura, and D. O. Boerma, "Growth and properties of Cu_3N films and Cu_3N/γ'-Fe_4N bilayers," Appl. Phys. Lett. **80**, 1823–1825 (2002).
13. G. H. Yue, P. X. Yan, J. Z. Liu, M. X. Wang, M. Li, and X. M. Yuan, "Copper nitride thin film prepared by reactive radio-frequency magnetron sputtering," J. Appl. Phys. **98**, 103506 (2005).
14. C. Gallardo-Vega and W. de la Cruz, "Study of the structure and electrical properties of the copper nitride thin films deposited by pulsed laser deposition," Appl. Surf. Sci. **252**, 8001–8004 (2006).
15. J. Wang, J. T. Chen, X. M. Yuan, Z. G. Wu, B. B. Miao, and P. X. Yan, "Copper nitride (Cu_3N) thin films deposited by RF magnetron sputtering," J. Cryst. Growth **286**, 407–412 (2006).
16. N. Gordillo, R. Gonzalez-Arrabal, M. S. Martin-Gonzalez, J. Olivares, A. Rivera, F. Briones, F. Agulló-López, and D. O. Boerma, "DC triode sputtering deposition and characterization of N-rich copper nitride thin films: Role of chemical composition," J. Cryst. Growth **310,** 4362–4367 (2008).
17. J. Xiao, Y. Li, and A. Jiang, "Structure, optical property and thermal stability of copper nitride films prepared by reactive radio frequency magnetron sputtering," J. Mater. Sci. Technol. **27**, 403–407 (2011).
18. K. Matsuzaki, T. Okazaki, Y. S. Lee, H. Hosono, and T. Susaki, "Controlled bipolar doping in Cu_3N (100) thin films," Appl. Phys. Lett. **105**, 222102 (2014).
19. C. M. Caskey, R. M. Richards, D. S. Ginley, and A. Zakutayev, "Thin film synthesis and properties of copper nitride, a metastable semiconductor," Mater. Horiz. **1**, 424–430 (2014).
20. G. Sahoo, S. R. Meher, and M. K. Jain, "Room temperature growth of high crystalline quality Cu_3N thin films by modified activated reactive evaporation," Mater. Sci. & Eng. B **191**, 7–14 (2015).
21. M. Birkett, C. N. Savory, A. N. Fioretti, P. Thompson, C. A. Muryn, A. D. Weerakkody, I. Z. Mitrovic, S. Hall, R. Treharne, V. R. Dhanak, D. O. Scanlon, A. Zakutayev, and T. D. Veal, "A typically small temperature-dependence of the direct band gap in the metastable semiconductor copper nitride Cu_3N," Phys. Rev. B **95**, 115201 (2017).
22. K. Matsuzaki, K. Harada, Y. Kumagai, S. Koshiya, K. Kimoto, S. Ueda, M. Sasase, A. Maeda, T. Susaki, M. Kitano, F. Oba, and H. Hosono, "High-mobility p-type and n-type copper nitride semiconductors by direct nitriding synthesis and in silico doping design," Adv. Mater. **30**, 1801968 (2018).
23. T. Yamaguchi, T. Yamaguchi, H. Nagai, H. Nagai, T. Kiguchi, N. Wakabayashi, T. Igawa, T. Hitora, T. Onuma, T. Honda, and M. Sato, "Epitaxial mist chemical vapor deposition growth and characterization of Cu_3N films on (0001)α-Al_2O_3 substrates," Appl. Phys. Express **13**, 075505 (2020).
24. A. K. Mukhopadhyay, Md. A. Momin, A. Roy, S. C. Das, and A. Majumdar, "Optical and electronic structural properties of Cu_3N thin films: A first-principles study (LDA+U)," ACS Omega **5**, 31918−31924 (2020).
25. C. A. Figueira, G. Del Rosario, D. Pugliese, M. I. Rodríguez-Tapiador, and S. Fernández, "Effect of argon on the properties of copper nitride fabricated by magnetron sputtering for the next generation of solar absorbers," Materials **15**, 8973 (2022).
26. E. Márquez, E. Blanco, M. García-Gurrea, M. Cintado Puerta, M. Domínguez de la Vega, M. Ballester, J. M. Mánuel, M. I. Rodríguez-Tapiador, and S. M. Fernández, "Optical properties of

reactive RF magnetron sputtered polycrystalline Cu_3N thin films determined by UV/visible/NIR spectroscopic ellipsometry: An eco-friendly solar light absorber," Coatings **13**, 1148 (2023).

27. S. Majumder, M. A. M. Patwary, K. Saito, Q. Guo, and T. Tanaka, "Fabrication of Cu_3N thin films on MgO(100) and α-Al_2O_3 (0001) substrates by reactive radio frequency magnetron sputtering: a comparative study," Jpn. J. Appl. Phys. **64**, 04SP34 (2025).
28. K. Wasa and S. Hayakawa, *Handbook of Sputter Deposition Technology: Principles, Technology and Applications* (Noyes Publication, New Jersey, 1992).
29. S. Woo, H. Choi, S. Kang, J. Lee, A. David, W. Prellier, Y. Kim, H. Y. Kim, and W. S. Choi, "Surface-orientation-dependent growth of $SrRuO_3$ epitaxial thin films," Appl. Surf. Sci. **499,** 143924 (2020).
30. T. Aizawa, S. Otani, I. Ohkubo, and T. Mori, "ZrC epitaxy on Si(111)," J. Vac. Sci. Technol. A **33**, 061512 (2015).
31. I. Ohkubo, T. Aizawa, K. M. Senados, M. S. L. Lima, T. Sakurai, and T. Mori, "Surface chemical states and structures of epitaxial Mg_2Sn thermoelectric thin films," Jpn. J. Appl. Phys. **62**, 108004 (2023).
32. G. E. Jellison and F. A. Modine, "Parameterization of the optical functions of amorphous materials in the interband region," Appl. Phys. Lett. **69**, 371–374 (1996).
33. P. Blaha, K. Schwarz, G. Madsen, D. Kvasicka, and J. Luitz, *WIEN2k, An Augmented Plane Wave + Local Orbitals Program for Calculating Crystal Properties*; TU Vienna: Vienna, Austria, 2001.
34. F. Tran and P. Blaha, "Accurate band gaps of semiconductors and insulators with a semilocal exchange-correlation potential," Phys. Rev. Lett. **102**, 226401 (2009).
35. D. Koller, F. Tran, and P. Blaha, "Merits and limits of the modified Becke–Johnson exchange potential," Phys. Rev. B **83**, 195134 (2011).
36. I. Ohkubo and T. Mori, "Comparative study of exchange–correlation functional and potential for evaluating thermoelectric transport properties in d^0 perovskite oxides," J. Phys. Soc. Jpn. **86**, 074705 (2017).
37. C. Tielemann, S. Reinsch, R. Maaß, J. Deubener, and R. Müller, "Internal nucleation tendency and crystal surface energy obtained from bond energies and crystal lattice data," J. Non-Cryst. Solids X **14**, 100093 (2022).
38. M. Holzer, T. Waurischk, J. George, R. Maaß, and R. Müller, "Silicate glass fracture surface energy calculated from crystal structure and bond-energy data," J. Non-Cryst. Solids **622**, 122679 (2023).
39. H. E. Swanson and E. Tatge, "Standard X-ray diffraction powder patterns," Natl. Bur. Stand. Circular **539**, 53–54 (1953).
40. P. Balliranoa and R. Caminiti, "Rietveld refinements on laboratory energy dispersive X-ray diffraction (EDXD) data," J. Appl. Cryst. **34**, 757–762 (2001).
41. R. H. Mitchell, A. R. Chakhmouradian, and P. M. Woodward, "Crystal chemistry of perovskite-type compounds in the tausonite–loparite series, $(Sr_{1-2x}Na_xLa_x)TiO_3$," Phys. Chem. Minerals **27**, 583–589 (2000).
42. S. W. Benson, "Bond energies," J. Chem. Educ. **42**, 502–518 (1965).
43. M. D. Morse, "Predissociation measurements of bond dissociation energies," Acc. Chem. Res. **52**, 119–126 (2019).
44. D. D. Wagman, W. H. Evans, V. B. Parker, R. H. Schumm, I. Halow, S. M. Bailey, K. L. Churney,

and R. L. Nuttall, "The NBS tables of chemical thermodynamic properties. Selected values for inorganic and C_1 and C_2 organic substances in SI units," J. Phys. Chem. Ref. Data **11**, Suppl. 2 (1982).

45. J. Wang, Z. Liu, Z. Dai, X. Song, and X. Liu, "Multifunctional catalytic activity of Cu_3N (001) surface: A first-principles study," ChemPhysMater **2**, 231–238 (2023).
46. A. J. Logsdail, D. Mora-Fonz, D. O. Scanlon, C. R. A. Catlow, and A. A. Sokol, "Structural, energetic and electronic properties of (100) surfaces for alkaline earth metal oxides as calculated with hybrid density functional theory," Surf. Sci. **642**, 58–65 (2015).
47. Dian-Na Zhang, Li Zhao, Jia-Fu Wang, and Yan-Li Li, "Electronic structures and the stability of MgO surface: density functional study," Surface Review and Letters **22**, 1550037 (2015).
48. J. Sun, T. Stirner, and A. Matthews, "Structure and surface energy of low-index surfaces of stoichiometric α-Al_2O_3 and α-Cr_2O_3," Surf. Coatings Technol. **201**, 4205–4208 (2006).
49. R. I. Eglitis and D. Vanderbilt, "First-principles calculations of atomic and electronic structure of $SrTiO_3$ (001) and (011) surfaces," Phys. Rev. B **77**, 1–10 (2008).
50. W. Liu, X. Liu, W. T. Zheng, and Q. Jiang, "Surface energies of several ceramics with NaCl structure," Surf. Sci. **600**, 257–264 (2006).
51. I. Ohkubo, H. M. Christen, S. V. Kalinin, G. E. Jellison, C. M. Rouleau, and D. H. Lowndes, "High-throughput growth temperature optimization of ferroelectric $Sr_xBa_{1-x}Nb_2O_6$ epitaxial thin films using a temperature gradient method," Appl. Phys. Lett. **84**, 1350–1352 (2004).
52. I. Ohkubo, Z. Hou, J. N. Lee, T. Aizawa, M. Lippmaa, T. Chikyow, K. Tsuda, and T. Mori, "Realization of closed-loop optimization of epitaxial titanium nitride thin-film growth via machine learning," Mater. Today Phys. **16**, 100296 (2021).
53. D. Depla and S. Mahieu, *Reactive Sputter Deposition* (Springer-Verlag Berlin Heidelberg 2008).
54. U. Hahn and W. Weber, "Electronic structure and chemical-bonding mechanism of Cu_3N, Cu_3NPd, and related Cu(I) compounds," Phys. Rev. B **53**, 12684–12693 (1996).
55. A. Zakutayev, C. M. Caskey, A. N. Fioretti, D. S. Ginley, J. Vidal, V. Stevanovic, E. Tea, and S. Lany, "Defect tolerant semiconductors for solar energy conversion," J. Phys. Chem. Lett. **5**, 1117−1125 (2014).
56. K. Seeger, *Semiconductor Physics: An Introduction (Advanced Texts in Physics)* (Springer-Verlag Berlin Heidelberg, 2004).
57. A. Modin, K. O. Kvashnina, S. M. Butorin, L. Werme, J. Nordgren, S. Arapan, R. Ahuja, A. Fallberg, and M. Ottosson, "Electronic structure of Cu_3N films studied by soft x-ray spectroscopy," J. Phys.: Condens. Matter **20**, 235212 (2008).
58. M. Yang, A. Zakutayev, J. Vidal, X. Zhang, D. S. Ginley, and F. J. DiSalvo, "Strong optical absorption in $CuTaN_2$ nitride delafossite," Energy Environ. Sci. **6**, 2994–2999 (2013).
59. A. Zakutayev, A. J. Allen, X. Zhang, J. Vidal, Z. Cui, S. Lany, M. Yang, F. J. DiSalvo, and D. S. Ginley, "Experimental synthesis and properties of metastable $CuNbN_2$ and theoretical extension to other ternary copper nitrides," Chem. Mater. **26**, 4970–4977 (2014).
60. I. Ohkubo and T. Mori, "Anisotropic anomalies of thermoelectric transport properties and electronic structures in layered complex nitrides AMN_2 (A = Na, Cu; M = Ta, Nb)," Chem. Mater. **27**, 7265–7275 (2015).
61. D. O. Scanlon, K. G. Godinho, B. J. Morgan, and G. W. Watson, "Understanding conductivity anomalies in Cu^I-based delafossite transparent conducting oxides: Theoretical insights," J. Chem. Phys. **132**, 024707 (2010).

62. J. Robertson, P. Peacock, M. Towler, and R. Needs, “Electronic structure of p-type conducting transparent oxides,” Thin Solid Films **411**, 96 (2002).

63. J. Vidal, F. Trani, F. Bruneval, Miguel A. L. Marques, and S. Botti, “Effects of electronic and lattice polarization on the band structure of delafossite transparent conductive oxides,” Phys. Rev. Lett. **104**, 136401 (2010).

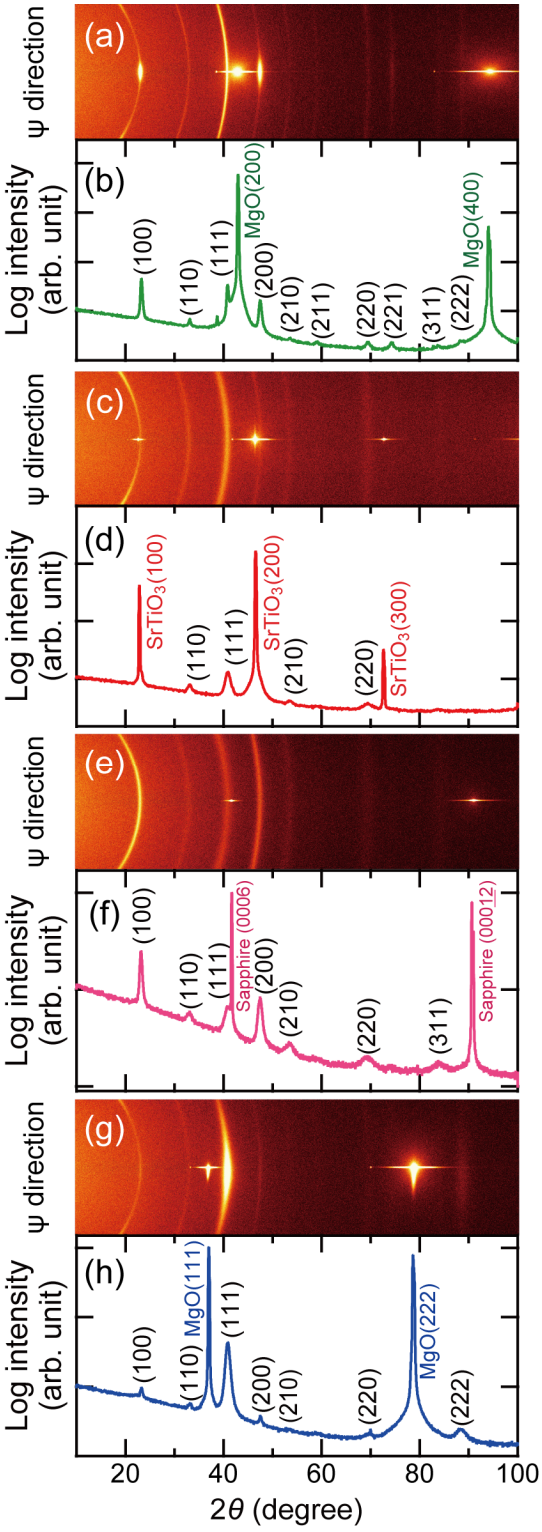

Fig. 1. (a),(c),(e),(g) XRD 2D images and (b),(d),(f),(h) 2θ–ω patterns of Cu_3N thin films grown with the following conditions and substrate: (a),(b) MgO(100) substrate at 170 °C growth temperature, DC power 25 W, nitrogen gas partial pressure (P_{N_2}) 1.7 Pa: (c),(d) $SrTiO_3$(100) substrate at 180 °C, 25 W, 1.7 Pa; (e),(f) sapphire(0001) substrate at 170 °C, 40 W, 1.7 Pa, and (g),(h) MgO(111) substrate at 180 °C, 25 W, 1.8 Pa. The vertical axis of XRD 2D images corresponds to the ψ direction.

Table 1. Surface energy values and parameters used for surface energy calculation: number of broken bonds per surface unit cell ($S_{(hkl)}$), coordination number of metal cation (*CN*), bond energy (D°), surface energy $\Upsilon_{(hkl)}$, and surface energy calculated using density-functional theory calculation (DFT) referred from the literature.

CF	Orientation	$S_{(hkl)}$	*CN*	D°(kJ/mol)	$\Upsilon_{(hkl)}$ (this study) (J/m^2)	$\Upsilon_{(hkl)}$(DFT) (J/m^2)
Cu_3N	(100)	1 [a]	2	235.53	2.69	0.123, 2.771 [b]
Cu_3N	(111)	3 [a]			4.64	0.394 [b]
MgO	(100)	2 [a]	6	166.43	6.23	0.92–1.03 [c] 1.37 [c]
MgO	(111)	3 [a]			10.79	2.04, 3.99 [d]
Sapphire (α-Al_2O_3)	(0001)	6 [a]	6	256.33	13.02	1.85 [e]
$SrTiO_3$	(100)	4 (Sr-O) 1 (Ti-O)	12 (Sr) 6 (Ti)	167.60 (Sr-O) 318.82 (Ti-O)	10.77	1.21, 1.29 [f]

[a] The numbers of broken bonds of the Cu plane and the Cu-N plane of Cu_3N(100), the Cu plane and the N plane of Cu_3N(111), the Mg plane and the O plane of MgO(111), the Al plane and the O plane of sapphire(0001), and the SrO plane and the TiO_2 plane of $SrTiO_3$(100) are, respectively, equal. [b] Ref. 45, [c] Ref. 46, [d] Ref. 47, [e] Ref. 48, [f] Ref. 49.

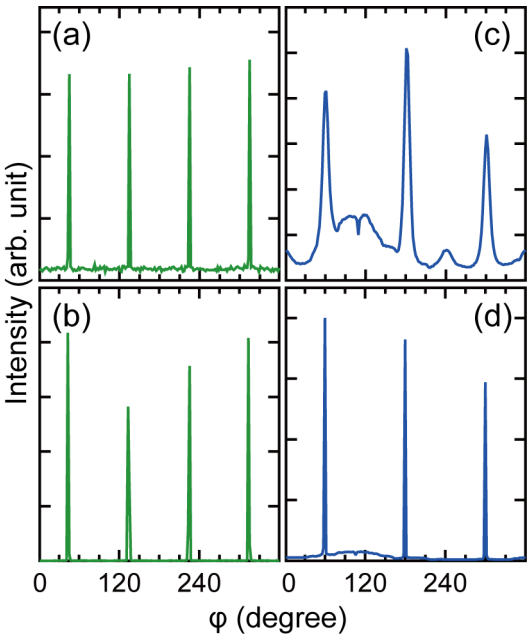

Fig. 2. XRD phi (φ) scan patterns of (a),(b) a Cu_3N thin film grown on a MgO(100) substrate and (c),(d) a Cu_3N thin film grown on a MgO(111) substrate. The measured diffraction planes are (a),(c) $Cu_3N\{111\}$ and (b),(d) MgO{111} for both on a MgO(100) substrate and on a MgO(111) substrate.

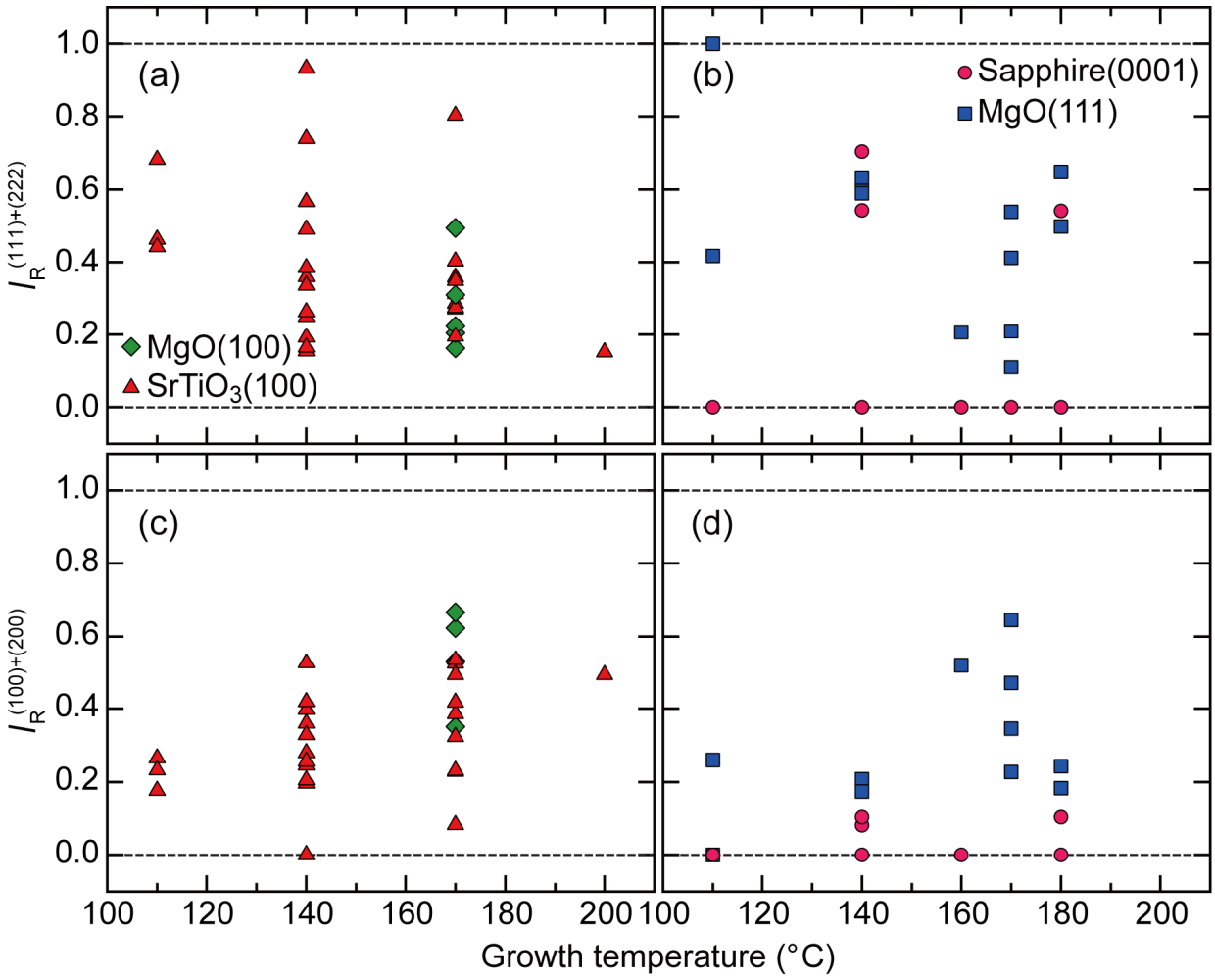

Fig. 3. (a),(b) Ratio ($I_R^{(111)+(222)}$) of the normalized XRD intensity $I_{norm}^{(111)}$ and $I_{norm}^{(222)}$ with $\Sigma I_{norm}^{(hkl)}$ shown as a function of growth temperature: (a) cubic symmetry surface unit cell substrates of MgO(100) and $SrTiO_3$(100); (b) rhombohedral symmetry surface unit cell substrates of sapphire(0001) and MgO(111). (c),(d) Ratio ($I_R^{(100)+(200)}$) of normalized XRD intensity $I_{norm}^{(100)}$ and $I_{norm}^{(200)}$ with $\Sigma I_{norm}^{(hkl)}$ shown as a function of growth temperature: (c) cubic symmetry surface unit cell substrates of MgO(100) and $SrTiO_3$(100); and (d) rhombohedral symmetry surface unit cell substrates of sapphire(0001) and MgO(111).

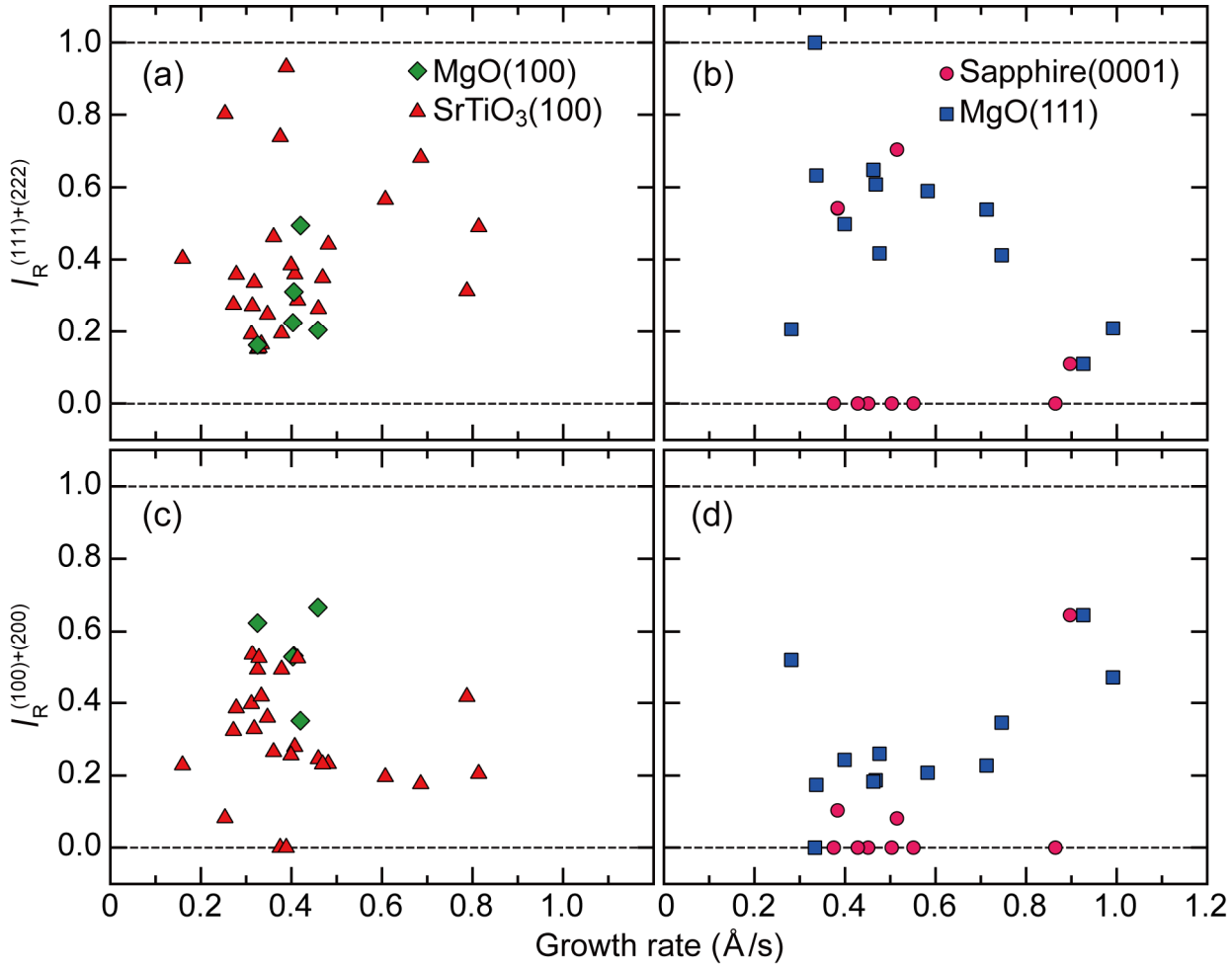

Fig. 4. (a),(b) Ratio ($I_R^{(111)+(222)}$) of the normalized XRD intensity $I_{norm}^{(111)}$ and $I_{norm}^{(222)}$ with $\Sigma I_{norm}^{(hkl)}$ shown as a function of growth rate: (a) cubic symmetry surface unit cell substrates of MgO(100) and $SrTiO_3$(100); (b) rhombohedral symmetry surface unit cell substrates of sapphire(0001) and MgO(111). (c),(d) Ratio ($I_R^{(100)+(200)}$) of normalized XRD intensity $I_{norm}^{(100)}$ and $I_{norm}^{(200)}$ with $\Sigma I_{norm}^{(hkl)}$ shown as a function of growth rate: (c) cubic symmetry surface unit cell substrates of MgO(100) and $SrTiO_3$(100); and (d) rhombohedral symmetry surface unit cell substrates of sapphire(0001) and MgO(111).

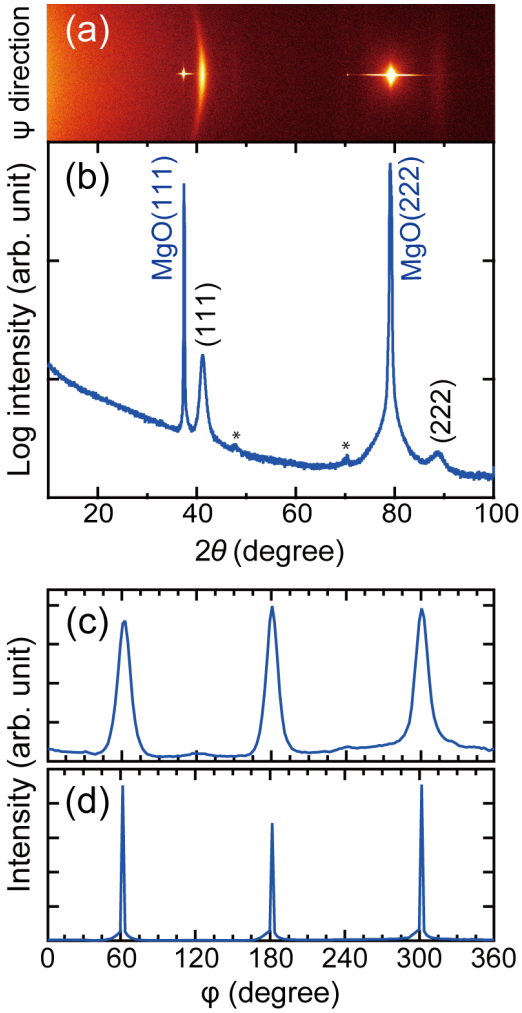

Fig. 5. (a) XRD 2D image, (b) 2θ–ω pattern, (c),(d) φ scan patterns of a single (111)-oriented Cu_3N epitaxial thin film grown on a MgO(111) substrate. The vertical axis of the XRD 2D image corresponds to the ψ direction. The asterisk * in Fig. 5 (b) denotes peak origination from the MgO(111) substrate, as shown in Fig. S4. The measured diffraction planes for φ scans are (c) Cu_3N{111} and (d) MgO{111}.

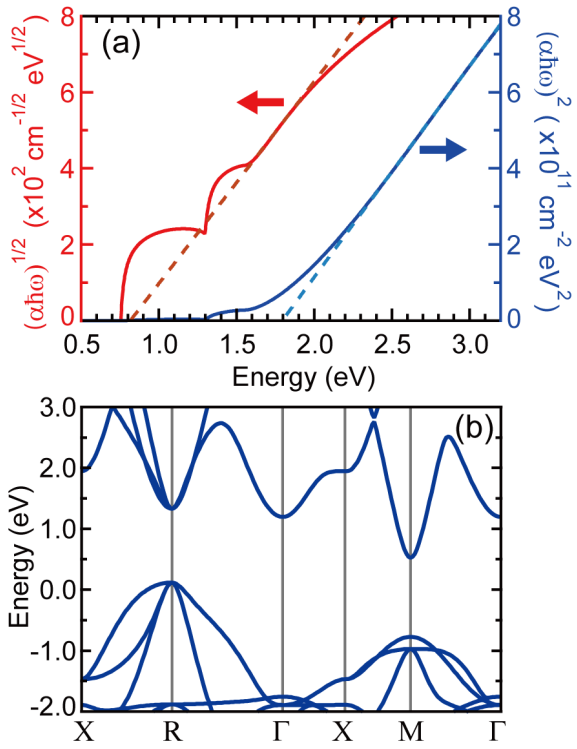

Fig. 6. (a) Optical absorption spectra of a single (111)-oriented Cu_3N epitaxial film grown on a MgO(111) substrate and (b) an electronic band structure of Cu_3N obtained using density-functional theory calculation using the mBJ exchange potential. In the optical absorption spectra, the $(\alpha\hbar\omega)^{1/2}$ versus $\hbar\omega$ plot is used for determination of the indirect energy band gap; also, the $(\alpha\hbar\omega)^2$ versus $\hbar\omega$ plot is used for calculation of the direct energy band gap. The labels in the Brillouin zone of electronic band structure Γ, X, R, and M respectively correspond to the following in lattice constant units: 0,0,0; 1,0,0; 1,1,1; and 1,0,1.